Modelling microseismicity of a producing reservoir from coupled fluid-flow and geomechanical simulation

D. A. Angus[1], J-M. Kendall[2], Q.J. Fisher[1], J.M. Segura[1,3], S. Skachkov[1,5], A.J.L. Crook[4] & M. Dutko[3]

[1]School of Earth & Environment, University of Leeds, Leeds, LS2 9JT, UK
[2]Department of Earth Sciences, University of Bristol, Bristol, BS8 1RJ, UK
[3]Rockfield Software Ltd., Swansea, SA1 8PH, UK
[4]Three Cliffs Geomechanical Analysis, Swansea, UK
[5]Now at Total Geoscience Research Center, Aberdeen, AB12 3FG, UK

Abstract:

In this paper, we investigate production induced microseismicity based on modelling material failure from coupled fluid-flow and geomechanical simulation. The model is a graben style reservoir characterised by two normal faults subdividing a sandstone reservoir into three compartments. The results are analysed in terms of spatial and temporal variations in distribution of material failure. We observe that material failure and hence potentially microseismicity is sensitive to not only fault movement, but also fluid movement across faults. For sealing faults, failure is confined to the volume in and around the well compartment, with shear failure localised along the boundaries of the compartment and shear-enhanced compaction failure widespread throughout the reservoir compartment. For non-sealing faults, failure is observed within and surrounding all three reservoir compartments as well as a significant distribution located near the surface of the overburden. All shear-enhanced compaction failures are localised within the reservoir compartments. Fault movement leads to an increase in shear-enhanced compaction events within the reservoir as well as shear events located within the side-burden adjacent to the fault. We also evaluate the associated moment tensor mechanisms to estimate the pseudo scalar seismic moment of failure based on the assumption that failure is not aseismic. The shear-enhanced compaction events display a relatively normal and tight pseudo scalar seismic moment distribution centered about 10^6 Pa, whereas the shear events have pseudo scalar seismic moments that vary over 3 orders of magnitude. Overall, the results from the study indicate that it may be possible to identify compartment boundaries based on the results of microseismic monitoring.

1.0 Introduction

Surface and subsurface geophones are being applied increasingly to monitor microseismic activity resulting from petroleum production. However, it is probably fair to state that those involved with microseismic monitoring have to some extent been struggling to identify the added value that such measurements provide. The most successful application has without a doubt been the use of the temporal and spatial variation in the location of microseismic events to monitor the propagation of *hydraulic fracturing*[†] that are artificially generated to both increase the rate of oil and gas production as well as to control *sand production* in poorly lithified reservoirs.

It has been argued that characterising the spatial and temporal variations in microseismicity can be used to assess changes in the stress field, and hence potentially be used to monitor perturbations in fluid pathways as well as *top seal* and *well bore integrity*. Furthermore, it has been suggested microseismicity can be used also to characterise spatial and temporal variations within the reservoir and surrounding rock mass by monitoring changes in seismic attributes between the source and receiver (e.g. shear-wave splitting analysis to characterise fracture induced anisotropy, Teanby et al., 2004). Furthermore, the evaluation of microseismic failure mechanisms can be used to characterise the rock mass at the source, such as providing a measure of the strength, orientation and type of elastic failure to potentially quantify damage (e.g. McGarr, 1971; Trifu et al., 2000; Anboori et al., 2006).

[†] definition of italised word given in Appendix A: Glossary.

Although microseismic analysis is often qualitatively helpful, quantitatively linking microseismicity to mechanical deformation and in-situ stress perturbations is not trivial. Hence, there is still considerable uncertainty regarding the potential future use of microseismic observations to increase the profitability of petroleum extraction. Generally, geomechanical models are calibrated by history matching with production data. Thus calibration is limited to discretely sampled regions of the model space (e.g. wellbore data). Microseismicity has the potential to provide information at distances from the well (e.g. monitoring changes in stress field and damage). However, calibration of microseismic data is needed to determine how much deformation is aseismic and hence undetectable using microseismic monitoring. Numerical prediction of geomechanical deformation and microseismicity is one approach to improve the link between observed microseismic attributes and mechanical deformation occurring throughout the reservoir, where calibration can be achieved by reducing the misfit between prediction and observation.

Recent studies linking fluid-flow, geomechanical and seismic modelling are enabling enhanced prediction of the subsurface response to fluid extraction, stress redistribution and mechanical deformation (e.g. Dean et al., 2003; Herwanger & Horne, 2005; 2009). Such tools can be used also to predict microseismicity and thus improve quantitatively the link between physical processes occurring within the reservoir to stress changes, rock failure and seismicity. A key aim of the work described in this paper is the use of coupled fluid-flow and geomechanical modelling to assess the potential of microseismic monitoring as a tool to assess reservoir compartmentalization. Two particular areas of interest are whether the distribution of microseismic activity could be used: (i) as an early indication of the level of reservoir compartmentalization and (ii) to identify the position of *compartment* boundaries. The latter could have significant economic benefits because *material balance calculations* conducted by the petroleum industry can often be used to show that production wells are in communication with far lower volumes of hydrocarbons than predicted based on static geological models. However, material balance calculations cannot be used

by themselves to identify the position of *unswept hydrocarbon*. If microseismic monitoring could be used to identify the position of compartment boundaries it would be possible to improve the positioning of infill wells to maximize further recovery.

In this paper, we develop a first-order approach to link coupled fluid-flow and geomechanical simulation with microseismic modelling. The paper begins by describing the coupled fluid-flow and geomechanical modelling tools as well as the specific geometry used during this study. We then go on to describe microseismic modelling technique that we have applied. Results from the modelling are then presented and discussed before conclusions are reached. It should be emphasized at the outset that this is a modelling exercise and that a key future activity will be to calibrate model predictions against real seismic data.

2.0 Coupled fluid-flow and geomechanical simulation

Current work in reservoir monitoring has focused on implementing coupled fluid-flow and geomechanical deformation modelling to improve our understanding of the subsurface response to hydrocarbon production (e.g. Dean et al., 2003). Commercial fluid-flow simulation packages are capable of modelling *multiphase fluid flow* (e.g. Aziz & Settari, 1979), but they generally neglect the influence of changing flow properties, such as pore pressure, on the mechanical behaviour of the reservoir and surrounding rock mass. Integrating changes in flow properties (e.g. changes in pressure and saturation) with geomechanical modelling vastly improves the prediction of dynamic changes within the reservoir and surrounding rock mass. Although formulations exist for fully coupled fluid-flow and geomechanical simulation, they tend to be computationally expensive (e.g. Minkoff et al., 2003). The sophistication of both commercial flow and geomechanical simulation algorithms makes iterative or loosely coupled flow-deformation algorithms highly attractive (e.g. Rutqvist et al., 2002; Settari & Sen, 2007). In this paper, we focus on the influence of production on stress redistribution and associated material failure. We refer to Lujun et al. (2006) and Kamitsuji et al. (2009) for examples of coupled fluid-flow and geomechanical simulation of hydraulic fracturing.

2.1 Numerical flow and geomechanical simulators

The coupled fluid-flow and geomechanical simulations are performed using an *iterative two-way coupling* scheme between the geomechanical solver ELFEN and the reservoir fluid-flow simulator MORE. The geomechanical solver ELFEN (developed by Rockfield Software Ltd.) is a finite-element/discrete-element solver for 2D and 3D problems. The reservoir simulator MORE (**M**odular **O**il **R**eservoir **E**valuation) is a commercial reservoir fluid-flow modelling package (TEMPEST software suite developed by Roxar). The coupling between ELFEN and MORE is achieved using a *message-passing interface*.

2.2 Constitutive models

The mechanical behaviour of rocks deviates significantly from perfect linear elasticity, where, for example, rocks are observed to be nonlinearly dependent on stress (e.g. Nur & Simmons, 1969). This stress dependence is generally attributed to the presence of compliant fractures and pores as well as grain boundary effects. Thus, accurate geomechanical modelling requires incorporation of such deviations from perfect linear elasticity. Normally this is achieved by modelling the material behaviour using *poroelastic* formulation or *constitutive model*.

The constitutive model used in the simulations is the so-called SR3 model, where the sandstone and shale characterisations are based on laboratory measurement of reservoir rocks. The SR3 model is a *critical state-based model* (Crook et al., 2006) and is calibrated using observed data from several confined triaxial experiments at large strains as well as a wide range of initial stress conditions. The model unifies shearing and consolidation properties of soil type material and can model *material hardening and softening* (i.e., the *failure surface* can evolve). Furthermore, the SR3 model has the added flexibility of incorporating elastic anisotropy, rate dependency and *creep* into the basic material characterization (Crook et al., 2002, 2006).

Figure 1 is a cartoon representation of the SR3 failure surface, highlighting the non-linear failure (yield) function. The failure surface is a function of the *effective mean stress* (p) and *deviatoric stress* (q) and is outlined (in 2-D space) by the blue curve. Four subdivisions

highlight the main failure regimes: tensile failure for $p \leq 0$, shear failure along the linear portion for $p \geq 0$, a transition from shear to *shear-enhanced compaction* along the apex of the curve, and shear-enhanced compaction (SEC) to the right (e.g. Fisher et al., 2007). For the special case of positive p and zero deviatoric stresses, the material undergoes pure *pore collapse*.

2.3 Model geometry

The geometry of the graben structure reservoir model is shown in Figure 2. The sandstone reservoir is geomechanically homogeneous and is located at approximately 3050 m depth, with dimension 6700 x 3350 m^2 laterally and height 76 m. In the *x*-direction, the reservoir is subdivided by two normal faults into three compartments; the end compartments having *x*-dimension 1675 m, and the middle compartment 3350 m. The middle compartment is slightly offset in depth by 38 m. The normal faults are inclined 60° from horizontal and have along strike and dip lengths of 3350 m and 850 m, respectively. The bounding volume consists of a shale type lithology with dimension 18900 x 9450 m^2 laterally and depth 3776 m. The shale is geomechanically homogeneous laterally. In all simulations, the production well is located vertically in the center of the left compartment.

A total of four simulations are performed with this geometry by varying the fault fluid sealing capacity as well as the fault plane *coefficient of friction*. The fault sealing capacity is defined using the fault *transmissibility multiplier* (TM) within the reservoir simulator, where a TM of 0.99 characterises a non-sealing fault and TM of 0.0001 characterises a *sealing fault*. The dynamic behaviour of the fault is defined by a cohesionless Mohr-Coulomb failure criterion for the fault contact elements using the coefficient of friction μ. For this particular geometry and the constitutive material models, μ = 0.750 results in the faults remaining locked throughout the simulation, whereas μ = 0.375 leads to fault movement of up to 1.5 m. The coefficient of friction is lower than the value used to separate conductive and non-conductive faults by studies such as Barton et al., (1995). However, the value of 0.375 is consistent with the low friction angles for clay-rich granular material (Plumb, 1994; Horsud, 2001) typical of fault rocks developed along seismic-scale faults (e.g. Fisher and Knipe, 1998; 2001, Manzocchi et al.,

1999). In all simulations, the well is produced at a constant rate of 4000 m³/d at a minimum well pressure of 5 MPa over a duration of approximately 10 years.

It should also be noted that we have assumed that fault movement does not increase fault permeability. This assumption is controversial in that several studies have indicated that active or critically stressed faults act as conduits for fluid flow. However, here we argue that this is often the case for faults developed in hard or over-consolidated rocks but that fault movement may occur without significantly increasing permeability when rocks have high porosity and are normally consolidated (e.g. Fisher et al., 2003).

3.0 Microseismic modelling

3.1 Integration with coupled flow-geomechanical results

The seismic link with the coupled flow-geomechanical simulation is achieved by passing various fluid and geomechanical parameters (e.g. pore pressure, static elasticity and stress tensor) via a so-called static results file at a user specified output frequency. For time-lapse seismic modelling, the output frequency can be set to mimic conventional surveys with output every year or so. For microseismic modelling, the output frequency can be increased to mimic as closely as possible a continuous monitoring scenario. In this paper, the static results are output approximately every 20 days. Note current research is focusing on implementing a continuous output scheme as well as other modifications discussed later in this paper.

3.2 Microseismic event distribution

Key in modelling microseismicity is the failure index that continuously monitors and flags whether a material point has experienced failure during simulation. Referring to Figure 1, the failure index can indicate no failure, where the evolution of the material stress-strain state has remained below the blue failure curve in *p-q space*. Otherwise, the material stress-strain state has reached the failure surface and has failed. The mode of failure can be characterised as: tensile failure (green), shear failure (blue), transition from shear to SEC failure (black) or SEC failure (red) (see Figure 1). If failure occurs, the location and relative time of failure is output to the static results file (along with the pre- and post-failure triaxial

confining stress tensor σ_{ij} and pore pressure P). The assumed microseismic event is flagged according to the type of failure to monitor the temporal and spatial evolution of the various modes of failure within the reservoir system.

3.3 Microseismic source and mechanism

The seismic source is commonly modelled as a distribution of body forces representing the transformation of elastic strain energy into propagating elastic strain energy. The so-called double-couple formulation is the most common source representation used, primarily because it can be computed relatively easily from seismic waveform data and yields relatively accurate estimates of failure. Since most microseismic events are often dominated by shearing components (Baker & Young, 1997), the double-couple solution is generally adequate approach for monitoring induced seismicity. However, analysis of non-shear components of failure using the seismic moment tensor representation have been used to study rock failure in greater detail, such as fracture initiation and type of failure (e.g. Feignier & Young, 1992).

We model the seismic source using a point-source seismic moment tensor representation, where non-shear components of failure, such as tensile and volumetric failure, can be simulated. We do this to allow for greater flexibility in the modelling algorithm as well as estimating the source magnitude at discrete node points when information on slip area and total slip is not available. Specifically, we adapt a microseismic waveform simulation algorithm developed for mine-induced microseismicity applications (Trifu et al., 2000) to reservoir monitoring applications.

Although the geomechanical solver ELFEN has the capability to evaluate fracture development, this would have introduced unnecessary complications into the model and is outside the scope of the current research. Thus given limited information regarding the geometry and dynamics of failure (e.g. slip area and total slip), we apply the approach of Zoback & Zoback (1980) who use the differential *effective stress* tensor $\Delta\sigma_{ij}$ as a first-order approximation of the failure mechanism. First, the pre- and post-failure effective stress tensor σ_{ij}^{pre} and σ_{ij}^{post} are evaluated using

$$\underline{\sigma}_{ij} = \sigma_{ij} - \alpha P \, \delta_{ij,}$$

$$(1)$$

where α is the *Biot coefficient* (here we assume $\alpha=1$ for simplicity) and δ_{ij} is the Kronecker delta function.   Next, the eigensolution of the diffential stress tensor $\Delta\sigma_{ij} = \underline{\sigma_{ij}}^{post} - \underline{\sigma_{ij}}^{pre}$ is evaluated to define the *P-, T- and B-axes*. The eigenvector associated with the maximum positive eigenvalue m_{max} corresponds to the *P*-axis and the minimum eigenvalue m_{min} to the *T*-axis.   The pseudo scalar seismic moment (or pseudo scalar moment) M_0 is evaluated as in Silver & Jordan (1982):

$$M_0 = (1/2)(m_1^2 + m_2^2 + m_3^2)^{1/2}. \qquad (2)$$

This approach is similar to that used by Hazzard & Young (2002), who model the seismic moment tensor from micromechanical particle models.   Here, the pseudo scalar moment estimate (2) has unit of force per area (e.g. N/m^2), whereas actual seismic moment has unit dyne-cm (or 10^{-7} N m). To scale the pseudo scalar moment estimate (2) to true seismic moment the surface area of failure (A), total slip (u) and shear modulus of fault (μ) are necessary (e.g. $M_0 = \mu u A$).   Another approach would be to characterise a seismic event based on the differential strain tensor (Daniel Moos, GMI, personal communication, March 2009).

4.0 Numerical Examples

Table 1 summarises the modelled events for all four simulations (see Appendix B for more details of model parameters). In terms of the total number of events, the cases with no fault movement yield essentially identical low numbers of roughly 17 thousands for the span of 10 years. In fact, for both the high and zero TM no fault movement examples, the results are essentially identical.   This alone would suggest that fault movement (i.e., lack of) plays a much greater role in controlling the stress state within and around the reservoir compared to the role of fluid movement (i.e., compartmentalisation). When fault movement occurs, the total number of modelled events is significantly larger, ranging between 40 and 70 thousand events.   This increase is mainly dominated by greater SEC failure within the reservoir. However, for the case of high TM and fault movement, there is the greatest number of modelled shear failure, indicating the fluid flow does play a significant role in microseismicity.

4.1 Fault movement

For the following two examples, the coefficient of friction $\mu = 0.375$ is sufficiently low to allow fault movement for the particular model geometry and constitutive material behaviour.

4.1.1 High transmissibility multiplier

In the first example, there is no restriction on fluid movement between all three reservoir compartments. Over the span of the production simulation, the faults are observed to slip a total of approximately 1.5 m. Figure 3 shows spatial distribution as well as pseudo scalar moment histogram plots for this example. Spatially, the events are evenly distributed along the *y*-axis, but it should be noted that events located close to the model boundaries are artifacts of the coarseness of the finite-element grid and boundary effects.   Along the *x*-axis, the SEC events display lateral heterogeneity, with a greater number of events occurring within the end compartments compared to central compartment.   The shear events appear to be confined to the edges of the reservoir with two peaks, one along the left side of the reservoir and the other located within the vicinity of the left fault. The depth histogram clearly indicates that the SEC events are confined to the reservoir (as expected) whereas the shear events are located along the outer boundary of the sandstone reservoir within the shale lithology as well as near the surface.

Also shown are event pseudo scalar moment histograms for both the SEC and shear type events.   The distribution for the SEC events have a normal distribution centered at approximately $10^{5.8}$.   The shear failure distribution is roughly trimodal with clusters around approximately $10^{4.7}$, $10^{5.4}$ and $10^{6.5}$. The shear events clustering at the lower pseudo scalar moments are those occurring in the near surface of the model, whereas those clustering at the higher pseudo scalar moments are events along the reservoir boundary (the over-/under- and side-burden).   The events clustering at the intermediate range pseudo scalar moment are those occurring in the side-burden volume within the vicinity of the faults.

In Figure 4, the temporal evolution of the event distribution is displayed.   Failure begins to initiate first as SEC type failure within the reservoir after roughly two years of production. Within a span of two years the number of SEC events begins to level off with event occurrence of approximately 750 events per month.   The

shear failure events lag the SEC events and initiate after roughly 6 years of production. The frequency of events appears to increase smoothly with time and do not appear to saturate. During the early stage of production, the SEC events are in the initial stages of initiation and seem to cluster in the regions near both normal faults.

4.1.2 Zero transmissibility multiplier

In this example, fluid movement is restricted to the left compartment where both faults act as impermeable barriers. Figure 5 displays the spatial and pseudo scalar moment distribution of modelled events. Similar to the previous example, the events are evenly distributed along the *y*-axis. However, along the *x*-axis, the events are confined to the volume surrounding the left reservoir compartment. This is because the volume of fluid extraction is limited to this compartment. As with the previous example, the SEC type events are confined to the reservoir itself whereas the shear events occur along the edges of the reservoir within the shale and with no events located near the surface. The reason why shear events do not occur in the near surface is because stress arching develops more efficiently around the smaller compacting volume compared to the High TM example. A consequence of the stress arching is the significant reduction in shear events located near the faults in the side-burden. The temporal evolution of microseismicity (Figure 6) is also similar to the previous example, except that it is characterised by lower event rates as well as a slightly longer delay in initiation of SEC and shear type events. This is a consequence of stress arching maintaining the excess load resulting from fluid extraction.

4.2 No fault movement

For the last two examples, the coefficient of friction $\mu = 0.750$ is sufficiently high to restrict fault movement for this particular model geometry and constitutive material behaviour.

4.2.1 High transmissibility multiplier

Figure 7 displays the spatial and pseudo scalar moment distribution of the modelled events. The distributions are generally similar to the case of high TM with fault movement. However, the differences lie in the absence of shear events near the model boundaries along the *y*-axis as well as within the vicinity of the faults (e.g. between 1000 and 3000 m along the

x-axis). The fact that near surface shear events are few and the lack of moderate pseudo scalar moment shear events within the side-burden near the faults suggest that stress arching has developed in this example (although not as efficiently as in the zero TM with fault movement example). This implies that fault movement can adversely affect the ability of the reservoir system to maintain stability during stress redistribution. Figure 8 shows the temporal evolution of the modelled events. The temporal distribution is similar to the high TM with fault movement example, except the time to reach SEC event saturation takes roughly an additional two more years.

4.2.2 Zero transmissibility multiplier

The results are virtually identical to the zero TM and fault movement example and so we refer to Figures 5 and 6.

5.0 Discussion

In this paper, we have assumed that all modelled material failure is microseismic (i.e., the mechanical failure will radiate elastic energy). However, material failure will not in general always lead to seismicity and may often be aseismic. If the strain rate of deformation is sufficiently low, strain within geomaterial can be accommodated by creep (e.g. Malservisi et al., 2005). To distinguish whether modelled material failure is seismic or aseismic, we can explore two approaches. The first approach involves monitoring the strain rate of failure and defining cut-off rate that characterises the boundary between seismic and aseismic failure (e.g. Malservisi et al., 2005). A second approach would involve monitoring the spatial and temporal location of material failure within a volume, selecting a criterion where events that cluster approximately linearly within a certain time span, and classifying the cluster as a composite microseismic event (e.g. Aker et al., 2009).

Another assumption in our approach involves estimating the moment tensor mechanism based on the change in the pre- and post-failure effective stress tensor (following Zoback & Zoback, 1980; Silver & Jordan, 1982; Hazzard & Young, 2002). Another possibility is to estimate the failure mechanism based on the change in the pre- and post-failure strain tensor since failure can also be considered due to a discontinuity in displacement. However, both the differential stress and strain approaches

assume that failure initiates in undamaged rock and the importance of preexisting material defects are ignored. For cases where slip occurs along preexisting zones of weakness having orientations that vary with respect with the principal effective stresses, the assumption that the *P*- and *T*-axes of the seismic failure mechanism is coincident with the true principal stress directions is generally not valid (e.g. Gephart & Forsyth, 1984). Thus an event location approach would be more suitable (e.g. Aker et al., 2009). Current research is directed at improving information passed from the coupled flow-geomechanical simulation algorithm for better modelling of failure. However, the approach discussed above represents a good first approximation of the microseismic source scalar seismic moment and mechanism when supplemental information, such as failure orientation and stress drop, are not available.

It is important to note that the location and pseudo scalar moment of the simulated microseismicity is model dependent. In terms of spatial dependence, the location of failure can only occur on the discrete mesh and so accurate modelling of microseismicity will be a function of grid density. As with any numerical discrete solution, for prediction of real data it is necessary to set the model up appropriately to obtain the required accuracy. The event pseudo scalar moments are sensitive to the temporal time step (e.g. large time steps will lead to larger pseudo scalar moments because larger stress changes can occur between each time step). However, the internal time steps taken by the geomechanical solver ELFEN are limited such that seismic waves can propagate across nodes between each time step.

Regardless of the simplicity of the model, the spatial and temporal as well as the pseudo scalar moment estimate distributions modelled in this paper have implications for real reservoir production scenarios. The SEC pseudo scalar moment and location distributions are symmetric and consistent between all model simulations, where the dominant mechanism of failure is pore collapse. This is because the effective stress in the reservoir is increasing due to pore pressure reduction and the weak material strength of the sandstone offers little resistance to pore collapse. The compacting reservoir influences the bounding shale because compaction requires the surrounding

shale to accommodate the stress perturbations. The events near the surface have small pseudo scalar moments (compare Figures 3 and 5 and note the absence of events in near subsurface as well as lower pseudo scalar moment shear events in Figure 5) and this is likely due to their distance from the region of stress redistribution as well as the lower material mechanical strength (i.e., Young's modulus is a function of the depth and porosity). The pseudo scalar moments of the events along the reservoir boundaries are highest because this is the region of stress arching (i.e., the region of the model that has had to take up the stress off loaded from the compacting reservoir). Within the results data file, it is observed that the events associated with the faults are moderate in pseudo scalar moment (compare Figures 3 and 7 and note the absence of moderate pseudo scalar moment shear events between $10^{5.5}$ and $10^{5.6}$ and lower number of shear events near left hand fault in Figure 7) and this is likely governed by the strength and motion of the fault. The symmetric Gaussian distribution of the pseudo scalar moments represents a typical size distribution of material matrix failure. It is important to stress that since we have no information regarding slip or area of failure (as these are point failures), we can only evaluate the pseudo scalar moment of point failure (e.g. the pseudo scalar moments are not earthquake magnitudes or moment magnitudes). The pseudo scalar moments discussed in this paper are essentially analogues to earthquake stress drop rather than moment magnitude. Thus the pseudo scalar moment distribution we model are similar to conventional earthquake static stress drop distributions (e.g. see figure 7a in Hardebeck & Aron, 2009).

6.0 Conclusions

We model production-induced microseismicity using coupled fluid-flow and geomechanical simulation for a graben reservoir model subdivided into three compartments by two normal faults. The results for this geometry indicate that fault movement as well as fluid extraction can influence the spatial, temporal and pseudo scalar moment of microseismicity. For sealing faults, microseismicity is located within the volume where fluid is extracted, with shear-enhanced compaction failure limited to the reservoir unit and shear failure along the boundaries of the sandstone reservoir. For non-sealing faults, shear-enhanced compaction

failure permeates through all three compartments as is expected for a fully compacting reservoir. Intuitively, fault movement leads to increased shear events within the side-burden near the fault. However, fault movement also enhances shear-enhanced compaction failure within the reservoir as well as a significant increase in shear events located within the near surface. The estimated pseudo scalar moments of the shear-enhanced compaction failure are relatively consistent and display normal distribution. The shear events display much more variability in pseudo scalar moment distribution. This variability is related to the spatial location of the event; low pseudo scalar moments in the near surface, moderate pseudo scalar moments in the side-burden near

the faults and high pseudo scalar moments for reservoir boundary shear events.

ACKNOWLEDGMENTS

References

Aker, E., H. Khoa, F. Cuisiat, and M. Soldal (2009) Acoustic emission experiments and microcrack modelling on porous rock, *EAGE: Passive Seismic: Case studies and applications for field development and exploration*, March, Limassol, Cyprus, 175-178.

Al-Anboori, A., J.-M. Kendall, D. Raymer, and R. Jones (2006) Spatial variations in microseismic focal mechanisms, Yibal Field, Oman, *EAGE Proceedings of the 68th Mtg.*

Aziz, K. and A. Settari (1979) *Petroleum reservoir simulation*, Applied Science Publishers Ltd., London.

Baker, C. and R. Young (1997), Evidence for extensive crack initiation in point source time-dependent moment tensor solutions, *B.S.S.A.*, **87**, 1442-1453.

Barton, C.A., M.D. Zoback and D. Moos (1995) Fluid flow along active faults in crystalline rocks, *Geology, 23, 683-686.*

Crook, A.J.L., J.-G. Yu, and S.M. Willson (2002) Development and verification of an orthotropic 3D elastoplastic material model for assessing borehole stability in shales, *SPE/ISRM Rock Mechanics Conference*, Irving, Texas, October 20-23, 78239.

Crook, A.J.L., S.M. Willson, J.-G. Yu, and D.R.J. Owen (2006) Predictive modelling of structure evolution in sandbox experiments, *Journal of Structural Geology*, **28**, 729-744.

Dean, R.H., X. Gai, C.M. Stone and S.E. Minkoff (2003) A comparison of techniques for coupling porous flow and geomechanics, *SPE*, 79709.

Feignier, B. and R. Young (1992) Moment tensor inversion of induced microseismic events: evidence of non-shear failures in the $-4 \leq m \leq -2$

moment magnitude range, *Geophys. Res. Lett.*, **19**, 1503-1506.

Fisher, Q.J. and R.J. Knipe (1998) Fault sealing processes in siliciclastic sediments. In G. Jones, Q.J. Fisher & R.J., Knipe. *Faulting and Fault Sealing in Hydrocarbon Reservoirs*. In *Special Publication of the Geological Society of London, 147*, 117-134.

Fisher, Q.J. and R.J. Knipe (2001) The permeability of faults within siliciclastic petroleum reservoirs of the North Sea and Norwegian Continental Shelf, *Marine and Petroleum Geology,* **18,** 1063–1081.

Fisher, Q.J., M. Casey, S.D. Harris and R.J. Knipe (2003) The fluid flow properties of faults in sandstone: the importance of temperature history. *Geology*, **31,** 965-968.

Fisher, Q., S. Harris, M. Casey, and R. Knipe (2007) Influence of grain size and geothermal gradient on the ductile-to-brittle transition in arenaceous sedimentary rocks: Implications for fault structure and fluid flow, *Geological Society of London, Special Publications*, 105-121.

Gephart, J. and D. Forsyth (1984) An improved method for determining the regional stress tensor using earthquake focal mechanism data: Application to the San Fernando earthquake sequence, *J. Geophys. Res.*, **B11**, 9305-9320.

Hardebeck, J.L. and A. Aron (2009) Earthquake stress drops and inferred fault strength on the Hayward Fault, East San Francisco Bay, California, *Bulletin of the Seismological Society of America*, **99**(3), 1801-1814.

Hazzard, J. and R. Young (2002) Moment tensors and micromechanical models, *Tectonophysics*, **356**, 181-197.

Herwanger, J.V. and S.A. Horne (2005) Predicting time-lapse stress effects in seismic data, *The Leading Edge*, **12**, 1234-1242.

Herwanger, J.V. and S.A. Horne (2009) Linking reservoir geomechanics and time-lapse seismics: Predicting anisotropic velocity changes and seismic attributes, *Geophysics*, **74**,W13-W33.

Horsud, P. (2001) Estimating mechanical properties of shale from empirical correlations. Society of Petroleum Engineers (SPE 56017), Drilling and Completion.

Kamitsuji, R., K. Nagai, Y. Matsuno, Y. Ohsaki, T. Tamagawa & K. Tezuka (2009) Hydraulic fracturing using heavy brine and microseismic monitoring in Yufutsu oil and gas field, SPE, 119358.

Lujun, J., A. Settari & R.B. Sullivan (2006) A new approach to hydraulic fracturing modelling – Fully coupled with geomechanical and reservoir simulation, SPE, 99428.

Malservisi, R., K. P. Furlong, and C. R. Gans (2005), Microseismicity and creeping faults: Hints from modeling the Hayward fault, California (USA), *Earth and Planetary Science Letters*, **234**, 421-435.

Manzocchi, T., J.J. Walsh, P. Nell and G. Yielding (1999) Fault transmissibility multipliers for flow simulation models. *Petroleum Geoscience,* **5,** 53–63.

McGarr, A. (1971), Violent deformation of rock near deep-level tabular excavations-seismic events, *B.S.S.A.*, **61**, 1453-1466.

Minkoff, S. E., C. M. Stone, S. Bryant, M. Peszynska, and M. F. Wheeler (2003), Coupled fluid flow and geomechanical deformation modeling, *Journal of Petroleum Science and Engineering*, **38**, 37-56.

Nur, A. and G. Simmons (1969), Stress-induced velocity anisotropy in rock: An experimental study, *J. Geophys. Res.*, **74**, 6667-6674.

Plumb, R.A. (1994) Variations of the least horizontal stress magnitude in sedimentary rocks. In: P.P. Nelson and S.E. Laubach, Editors, *Rock Mechanics: Models and Measurements, Challenges from Industry*, 71–78, Balkema, Rotterdam.

Rutqvist, J., Wu, Y.-S., Tsang, C.-F., and Bodvarsson, G. (2002) A modeling approach for analysis of coupled multiphase fluid flow, heat transfer, and deformation in fractured porous rock, *International Journal of Rock Mechanics & Mining Sciences*, **39**, 429-442.

Settari, A.T. and Sen, V. (2007) The role of geomechanics in integrated reservoir modeling, *The Leading Edge*, **26**(5), 622-627.

Silver, P. and T. Jordan (1982), Optimal estimation of scalar moment, *Geophys. J. R. astr. Soc.*, **70**, 755-787.

Teanby, N., J.-M. Kendall, R. H. Jones, and O. I. Barkved (2004), Stress-induced temporal variations in seismic anisotropy observed in microseismic data, *Geophys. J. Int.*, **156**, 459-466.

Trifu, C.-I., D. A. Angus, and V. Shumila (2000), A fast evaluation of the seismic moment tensor for induced seismicity, *B.S.S.A.*, **90**(6), 1521-1527.

Zoback, M. and M. Zoback (1980), State of stress in the conterminous United States, *J. Geophys. Res.*, **85**, 6113-6156.

TABLES:

Model		Total	Shear	SEC	Transitional
TM	**Fault**				
High	Movement	66,367	18,036	48,163	168
Zero	Movement	41,861	2,092	39,754	15
High	No movement	17,776	1,603	16,084	89
Zero	No movement	17,719	1,574	16,055	90

Table 1: Summary of failure events for each model simulation: TM refers to transmissibility multiplier (high=99% and zero=0.01%), Shear refers to pure shear events, SEC refers to shear enhanced compaction events (i.e., close to pore collapse) and Transitional refers to events undergoing a mixture of shear and shear enhanced compaction.

FIGURES:
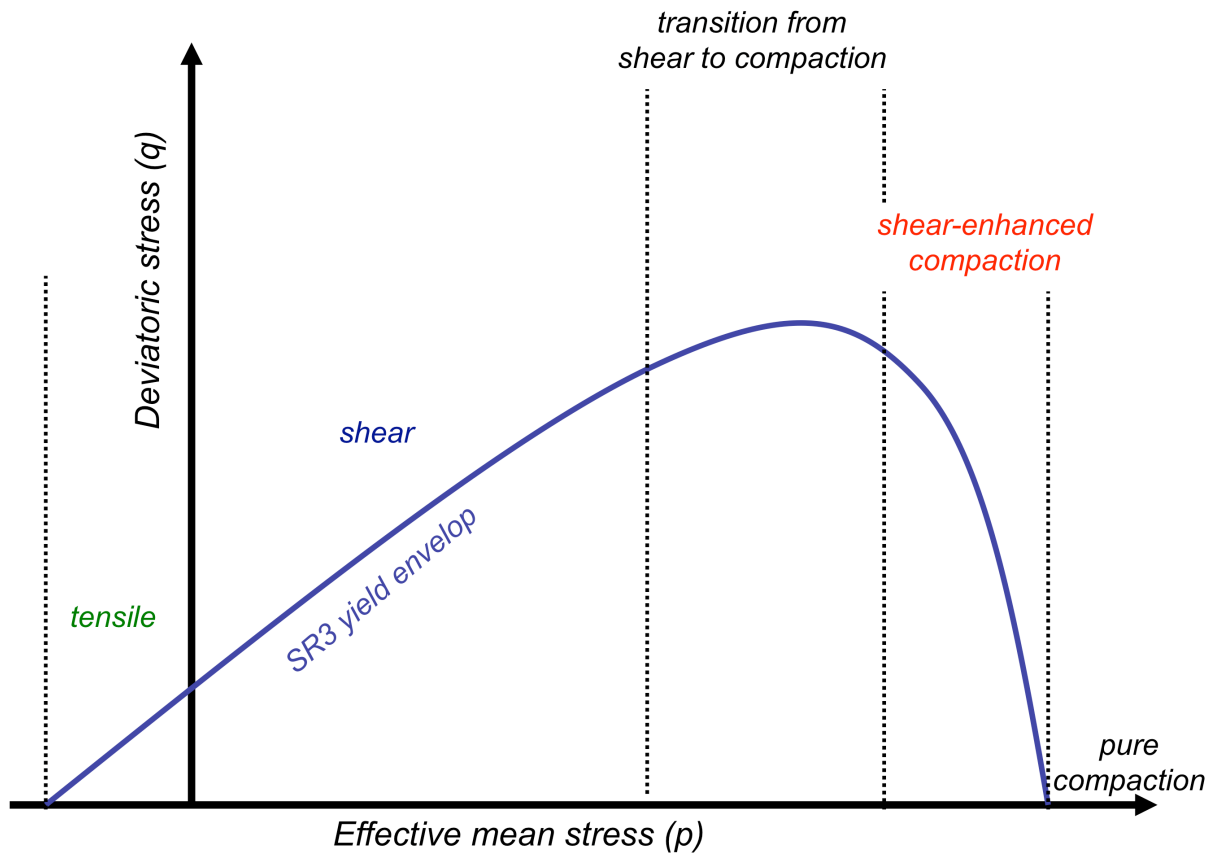
Figure 1: Schematic diagram highlighting the SR3 model. The blue yield surface defines the boundary between plastic (irreversible) and elastic rock deformation. The main types of failure are tensile (green) when the mean effective stress (*p*) is negative, shear (blue) when *p* is greater than zero but still moderate, shear–enhanced compaction (red) when *p* is sufficiently large allowing some pore collapse (grain–boundary compaction) during shear failure, and pure compaction (black) when *p* is at a maximum and only pore collapse/grain compaction occurs.
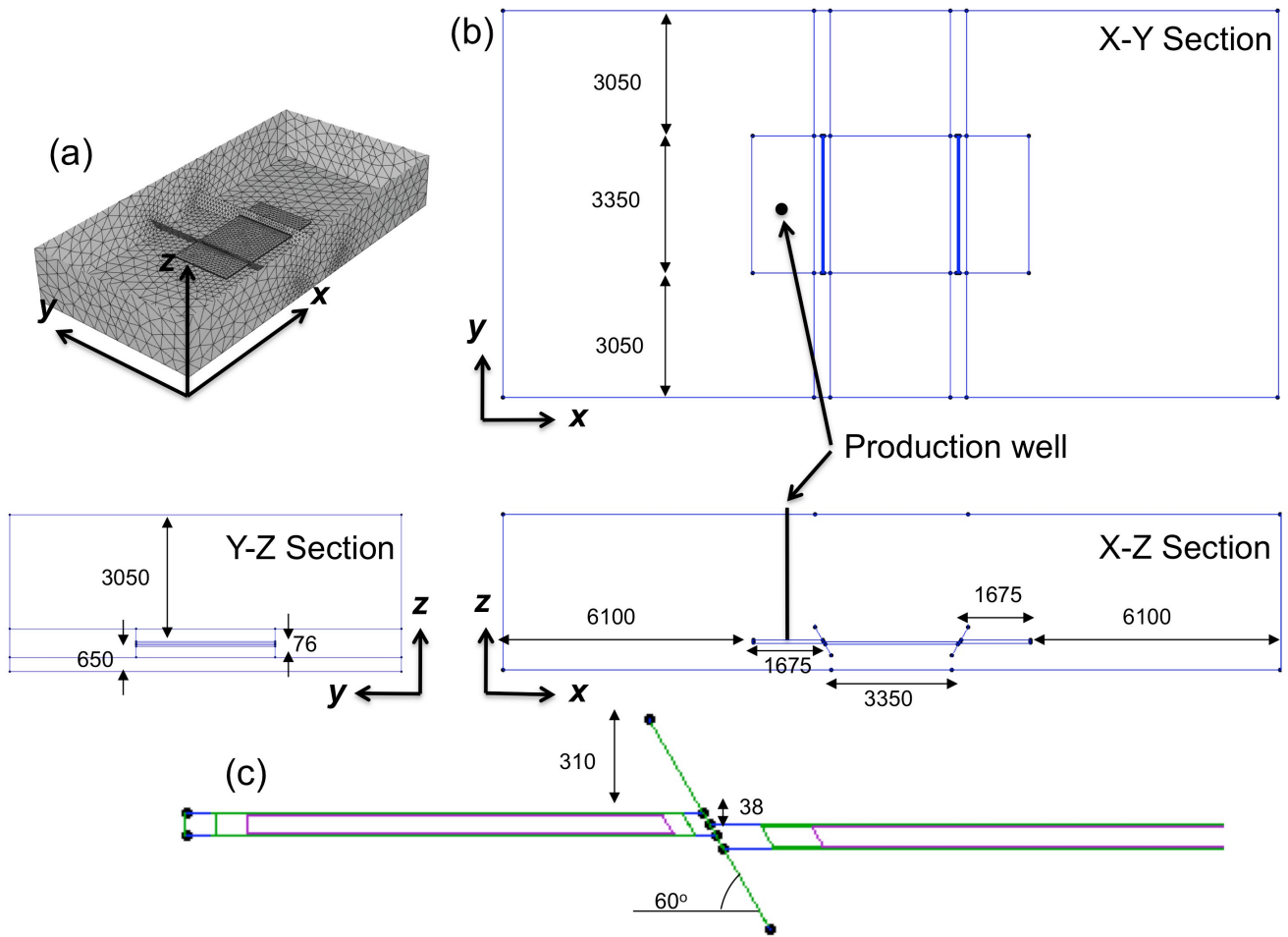
Figure 2: Geometry of the graben sandstone reservoir model (all spatial units are in meters and fault angle is degree from horizontal). The unstructured finite-element mess used in the geomechanical simulation is illustrated in (a). The three plots in (b) show the outline of the two fault sandstone reservoir geometry: (clockwise from top right) horizontal section with well defined by black dot in left compartment; vertical section through all three compartments with well defined by vertical black line on left compartment; and vertical section along of outer compartment. The bottom plot (c) is a detailed view of the fault geometry.
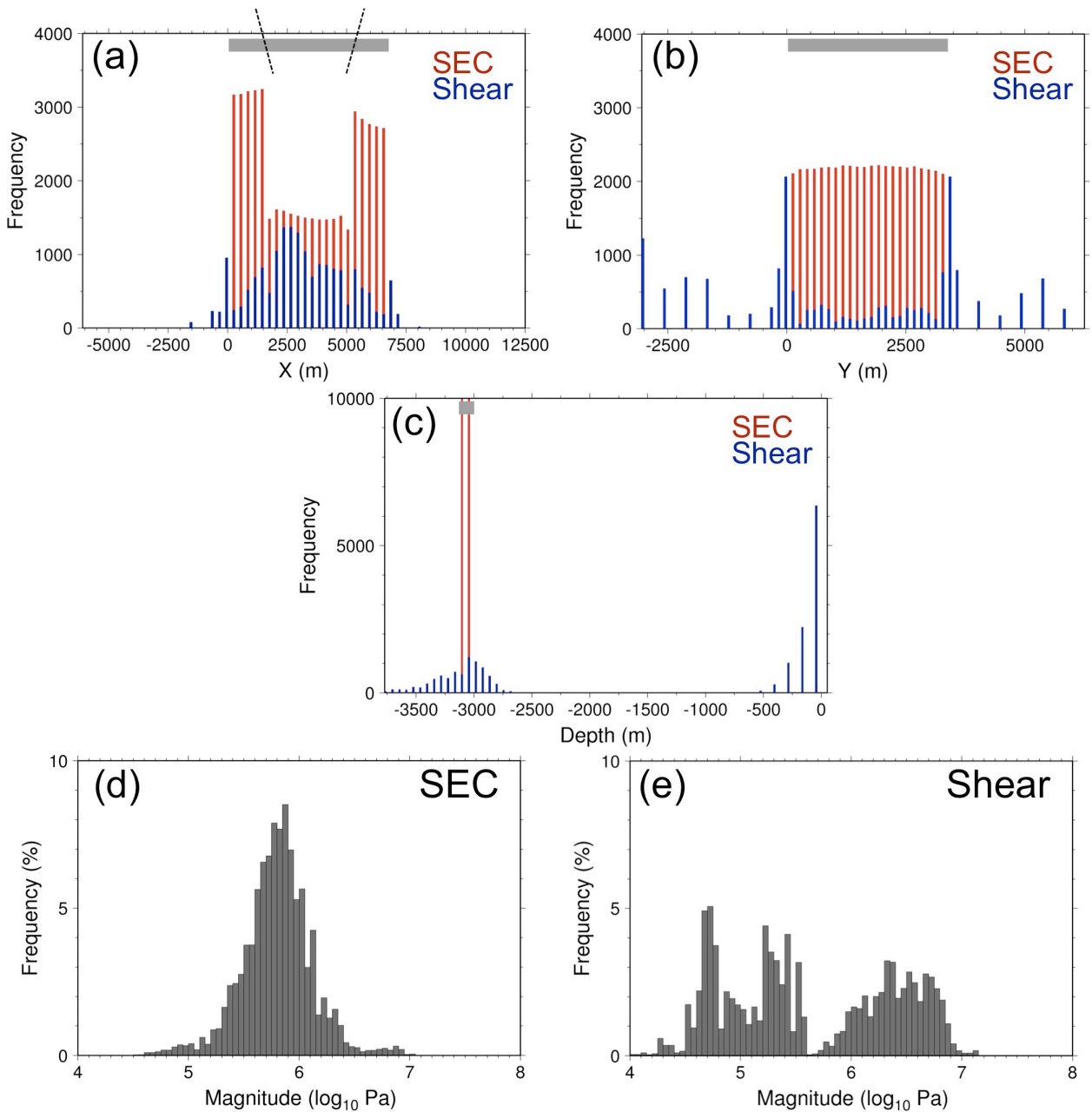
Figure 3: Spatial microseismic distribution and pseudo scalar moment histograms for high TM and fault movement example: spatial distribution in *x* (a), *y* (b) and depth (c). In this figure (as well as Figures 5 and 7) red represents shear–enhanced compaction and blue shear failure. The grey rectangle represents the extent of the reservoir in each section and the dashed inclined lines the location of the normal faults. The pseudo scalar moment distribution is shown in (d) for shear–enhanced compaction failure and (e) for shear failure.
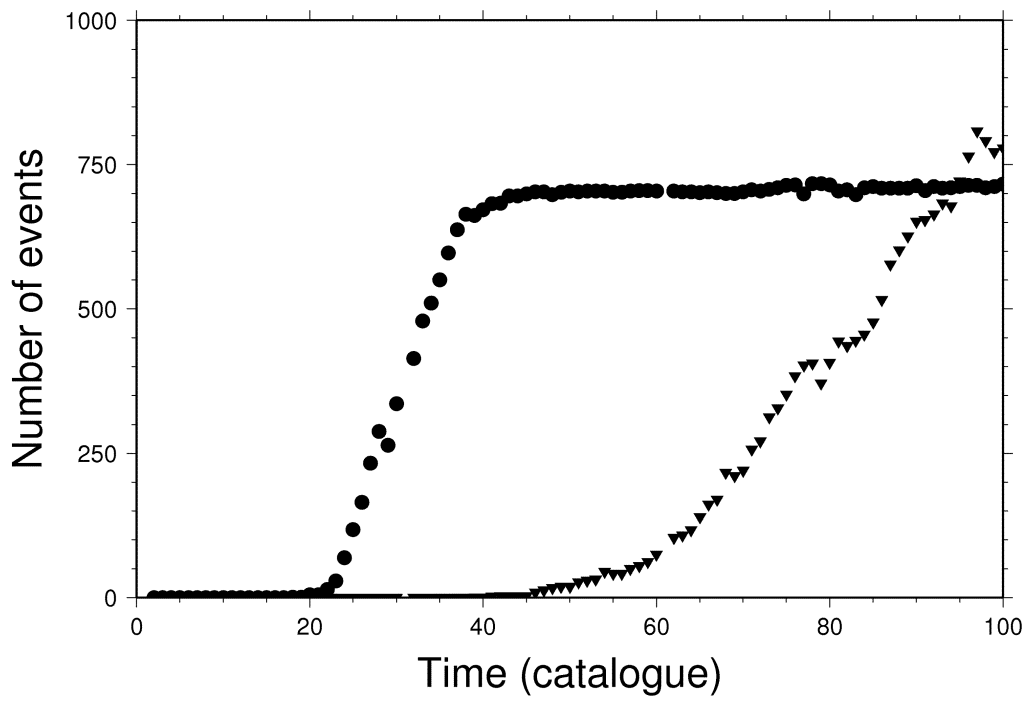
Figure 4: Temporal microseismic distribution for high TM and fault movement example: (circles) shear-enhanced compaction and (inverted triangles) shear events.
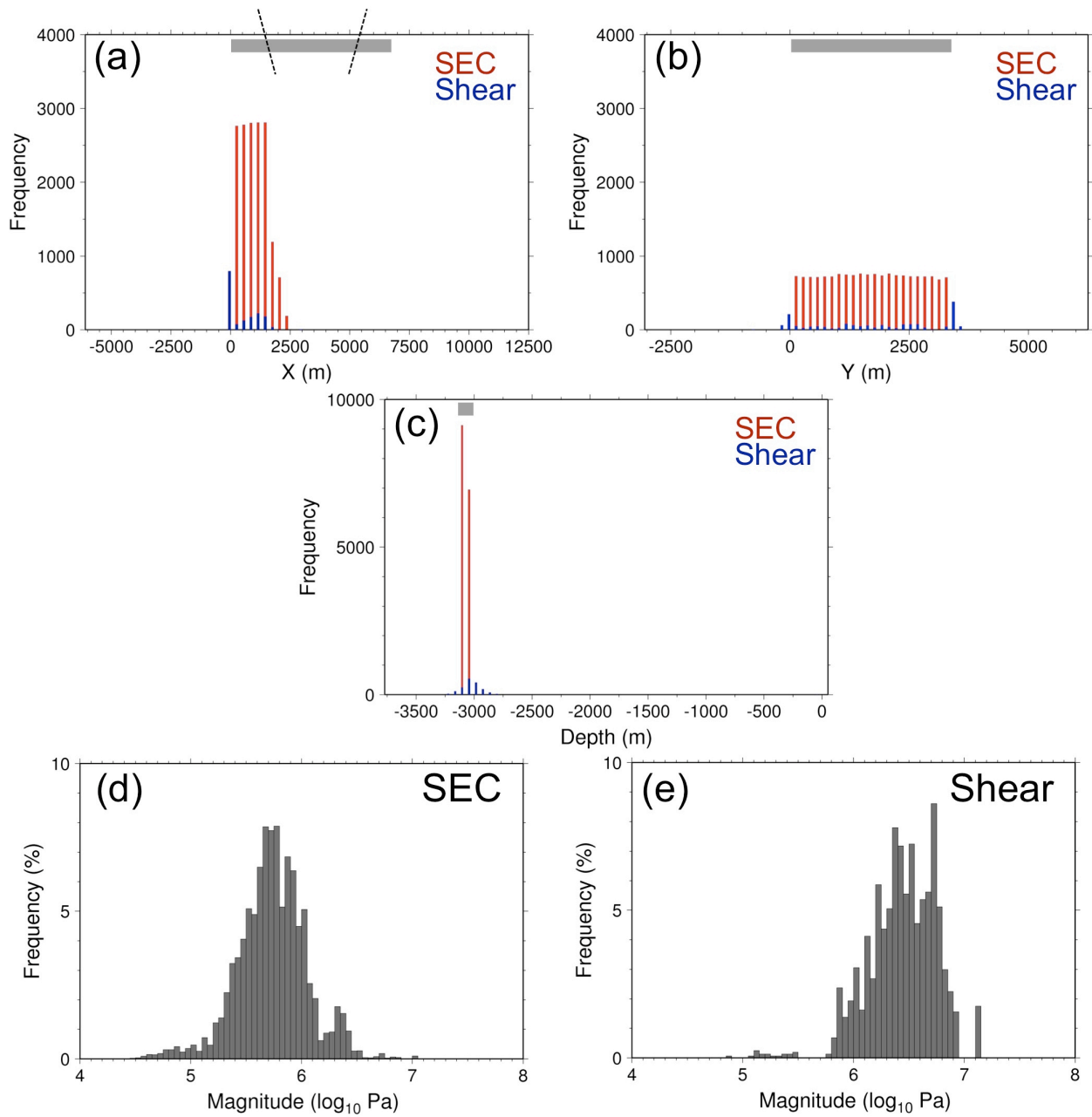
Figure 5: Spatial microseismic distribution and pseudo scalar moment histograms for zero TM and fault movement example (see caption in figure 3 for details).
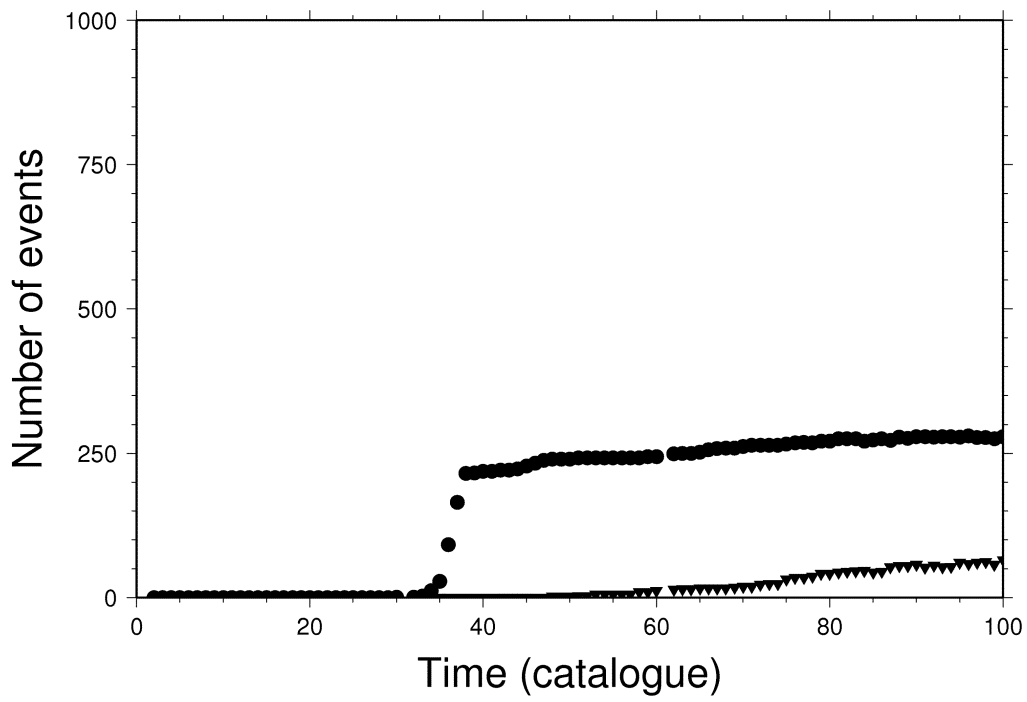
Figure 6: Temporal microseismic distribution for zero TM and fault movement example: (circles) shear-enhanced compaction and (inverted triangles) shear events.
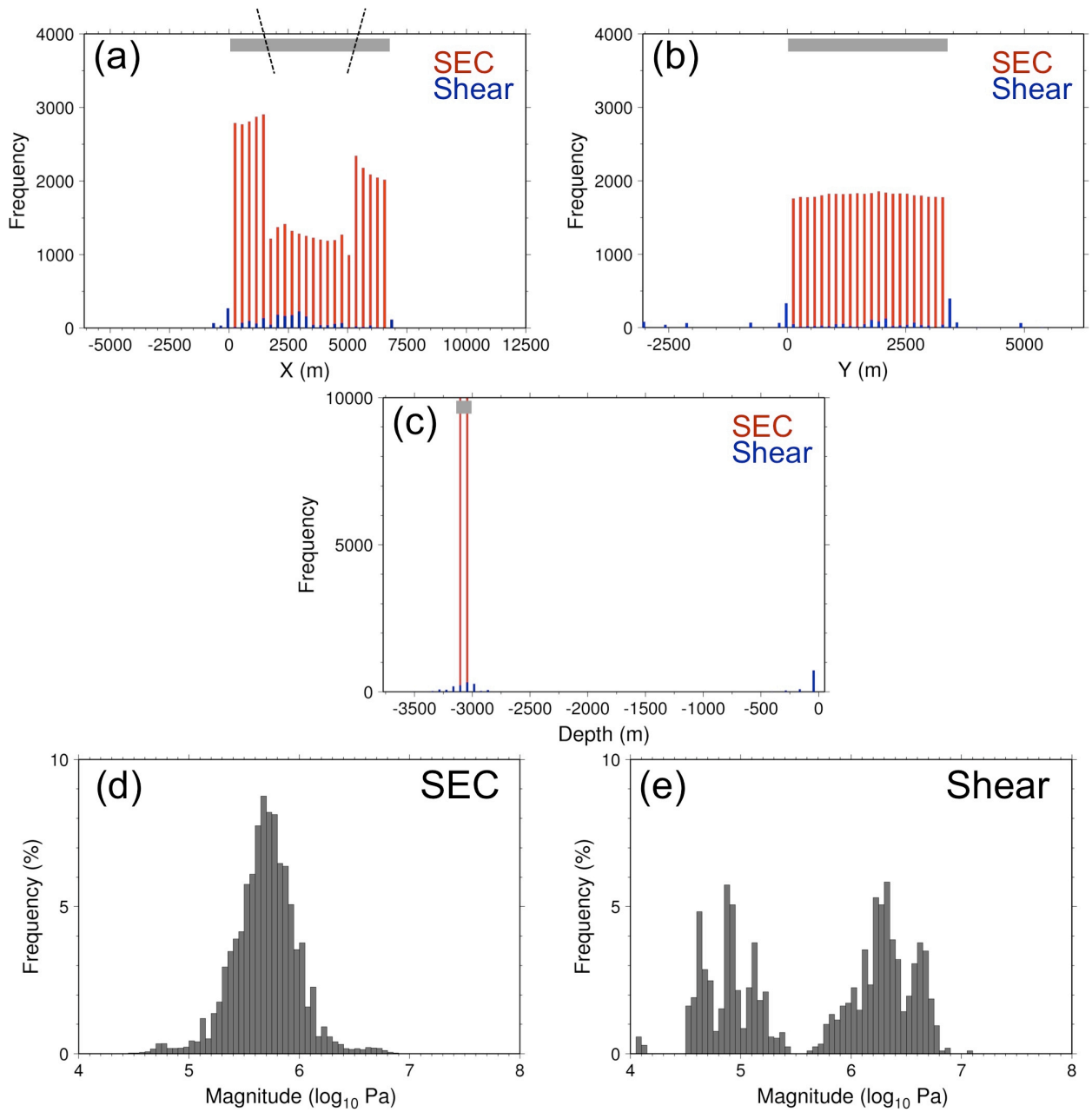
Figure 7: Spatial microseismic distribution and pseudo scalar moment histograms for high TM and no fault movement example (see caption in figure 3 for details).
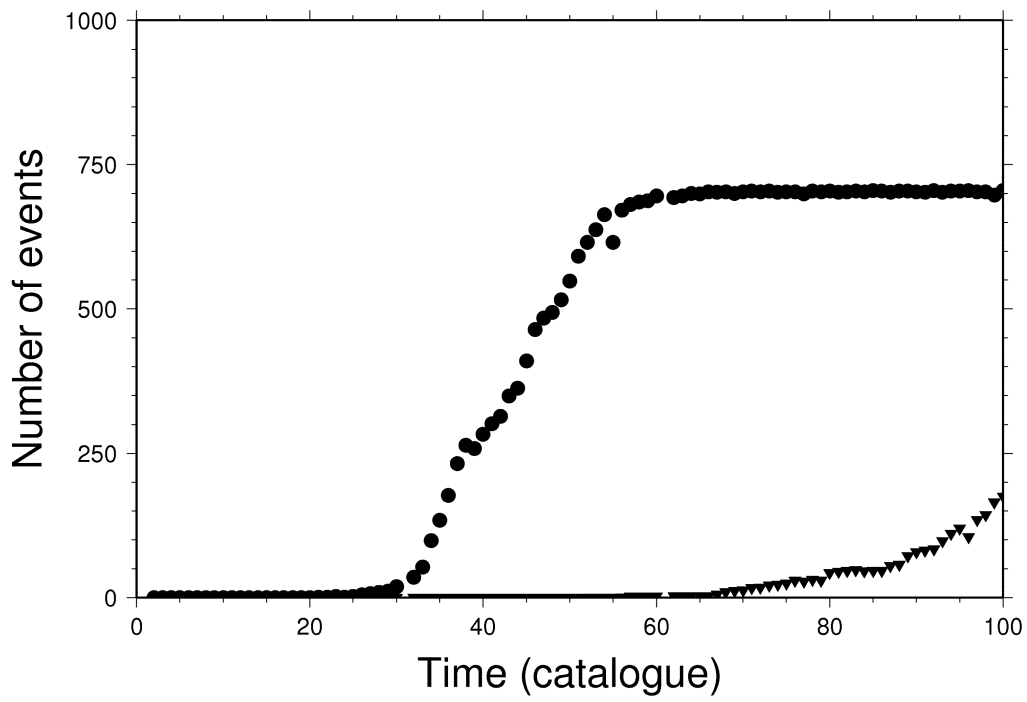
Figure 8: Temporal microseismic distribution for high TM and no fault movement example: (circles) shear-enhanced compaction and (inverted triangles) shear events.

Appendix A: Glossary:

Biot coefficient (α): coefficient that relates the influence of pore pressure on the total effective stress – used for calculating the impact of pore pressure changes on volume.

Coefficient of friction (μ): relates the shear stress needed to overcome the normal stress acting on a surface in order for sliding to occur.

Compartment: sub-volume of reservoir where fluid and pressures are partially or totally isolated from the rest of the reservoir.

Constitutive model: model for the mechanical behaviour of material.

Creep: slow and permanent deformation of solid material.

Critical state-based model: an elastoplastic constitutive model where, i) a critical state surface (or line) in the p-q plane, defines an effective stress state where unrestricted, constant-volume plastic flow occurs at constant effective stress, and ii) strain-hardening/softening is defined by a relationship between consolidation pressure and volumetric strain.

Deviatoric stress (q): hydrostatic stress subtracted from the total stress tensor.

Effective mean stress: the mean value of the three principal stresses of the effective stress tensor.

Effective stress tensor (σ_{ij}): total stress tensor minus pore pressure (pore pressure is scaled by the effective stress coefficient).

Failure surface: surface in deviatoric and normal stress space defining the boundary where irreversible deformation takes place.

Fault transmissibility multiplier (TM): fraction describing the fault permeability, ranging between 1 (100% non-sealing) and 0 (100% sealing). This is an average parameter characterising the flow properties of a fault.

Hydraulic fracturing: artificial stimulation of fractures using.

Hydrostatic stress: is an isotropic stress (i.e., where vertical and the two horizontal stresses are equal) and is given by the weight of the material above a certain point.

Iterative two-way coupling: approach for integrating two numerical algorithms using thresholds levels to dictate when information is passed between the programs.

Material balance calculations: estimating hydrocarbon reserves using pressure analysis as fluids are withdrawn.

Material softening and hardening: brittle or plastic deformation of material resulting in either weakening (strain softening) or strengthening (strain hardening) of the material

Message-passing interface: technique that allows two or more computer programs to communicate with one another via RAM (i.e., does not require storing information to disk).

Multiphase fluid-flow: flow characteristics when two or more immiscible fluids are present within a porous medium.

Pore collapse: significant and irreversible reduction in pore volume.

Poroelastic: an elastic medium having porosity and containing a viscous fluid.

p-q space: coordinate space defined by horizontal axis given by $p=(\sigma_1+\sigma_3)/2$ and vertical axis by $q=(\sigma_1-\sigma_3)/2$, where σ_1 and σ_3 are the maximum and minimum principal stresses.

P-,T- and B-axis: The P and T axis represent the maximum and minimum compressive stress directions, respectively, for a double-couple failure mechanism. The B-axis is the intermediate compressive stress direction and is zero for pure double-couple failure.

Sand production: undesirable flow of sand with fluid production that can lead to erosion to infrastructure.

Sealing fault: fault acting as a barrier to flow directions along and/or across the fault surface.

Shear-enhanced compaction: compaction that results from application of a deviatoric stress and occurs at lower stress values than needed for compaction when only a hydrostatic stress is applied.

Top seal: lithological unit of rock above reservoir acting as a barrier to upward migration of fluid.

Un-swept hydrocarbon: volume of hydrocarbon inaccessible to enhanced oil and gas production.

Well bore integrity: maintaining the integrity of a wellbore with optimum mud weight within the upper and lower pressure limits.

Appendix B: Geomechanical and reservoir flow parameters:

The constitutive model for the bounding shale and sandstone reservoir is the same (SR3) but with different model parameters (i.e., the shale is stronger than the sandstone). The shale porosity (ϕ^{shale}) versus depth (z) trend is expressed

$\phi^{shale}=1-(z/6.02)^{1/6.35}$,

where the Young's modulus (E^{shale}) is defined
$E^{shale}=21.4\phi^{-0.37}$,
with Poisson's ratio (v^{shale}) of 0.45.
The sandstone reservoir porosity (ϕ^{ss}) versus depth (z) trend is expressed
$\phi^{ss}=0.418-0.066z$,
where the Young's modulus (E^{ss}) is defined
$E^{ss}=13.8\phi^{-0.4}$,
with Poisson's ratio of (v^{ss}) of 0.25. The consistency of these parameters with real data is discussed in Crook et al. (2002,2006). The residual friction angle is approximately 38^0 in both materials, but the consolidation pressure is higher for the bounding shale material. For the sandstone the initial consolidation pressure is approximately 35 MPa and for the shale is approximately 55 MPa.

The boundary conditions for the finite element model are roller type boundaries (i.e., prescribed displacement normal to the boundaries). Before production a geostatic stage is considered where the initial stress state is applied to the model. Specifically, vertical stress is equal to the weight of the material (gravity is accounted for), an isotropic initial horizontal stress is defined where the ratio of horizontal to vertical stress is 0.5, and the initial stress state is elastic (i.e., plastic deformation only occurs during production).

Gas production is performed at the same rate for all cases. However, due to the different recoverable volumes, production is performed during 4000 days for the zero TM case and 8000 days for the high TM case. In all cases, the geostatic initialisation step is performed for 1000 days prior to production.

Erratum

Modelling microseismicity of a producing reservoir from coupled fluid-flow and geomechanical simulation

D. A. Angus[1], J-M. Kendall[2], Q.J. Fisher[1], J.M. Segura[1,3], S. Skachkov[1,5], A.J.L. Crook[4] & M. Dutko[3]

[1]School of Earth & Environment, University of Leeds, Leeds, LS2 9JT, UK
[2]Department of Earth Sciences, University of Bristol, Bristol, BS8 1RJ, UK
[3]Rockfield Software Ltd., Swansea, SA1 8PH, UK
[4]Three Cliffs Geomechanical Analysis, Swansea, UK
[5]Now at Total Geoscience Research Center, Aberdeen, AB12 3FG, UK

The authors of the paper above would like to highlight some errors that were not transferred correctly by the publisher at proof correction stage:

In the Model Geometry section, the sentence:

The dynamic behaviour of the fault is defined by a cohesionless Mohr-Coulomb failure criterion for the fault contact elements using the coefficient of friction m.

should read:

The dynamic behaviour of the fault is defined by a cohesionless Mohr-Coulomb failure criterion for the fault contact elements using the coefficient of friction μ.

Equation 2 describing the pseudo scalar seismic moment M_0 should read

$$M_0 = [(m_1^2 + m_2^2 + m_3^2)/2]^{1/2}.$$

In the Discussion section, the sentence:

Within the results data file, it is observed that the events associated with the faults are moderate in pseudo scalar moment (compare Figs 3 and 7 and note the absence of moderate pseudo scalar moment shear events between 105.5 and 105.6 and lower number of shear events near left hand fault in Fig. 7) and this is likely governed by the strength and motion of the fault.

should read:

Within the results data file, it is observed that the events associated with the faults are moderate in pseudo scalar moment (compare Figs 3 and 7 and note the absence of moderate pseudo scalar moment shear events between $10^{5.5}$ and $10^{5.6}$ and lower number of shear events near left hand fault in Fig. 7) and this is likely governed by the strength and motion of the fault.

References

Angus, D.A., J-M. Kendall, Q.J. Fisher, J.M. Segura, S. Skachkov, A.J.L. Crook and M. Dutko (2010) Modelling microseismicity of a producing reservoir from coupled fluid-flow and geomechanical simulation, *Geophysical Prospecting*, **58**(5), 901-913.